Observations of Coherent Turbulence Structures in the Near-Neutral Atmospheric Boundary Layer

Mitsuaki Horiguchi · Taiichi Hayashi ·
Hiroyuki Hashiguchi · Yoshiki Ito · Hiromasa Ueda

M. Horiguchi · T. Hayashi

Disaster Prevention Research Institute, Kyoto University, Gokanosho, Uji, Kyoto, Japan

e-mail: horiguchi@storm.dpri.kyoto-u.ac.jp

H. Hashiguchi

Research Institute for Sustainable Humanosphere, Kyoto University, Uji, Kyoto, Japan

Y. Ito

Sonic Corporation, Tokyo, Japan

H. Ueda

Japan Environmental Sanitation Center, Kawasaki, Kanagawa, Japan

Abstract   Turbulence structures of high Reynolds number flow in the near-neutral atmospheric boundary layer (ABL) are investigated based on observations at Shionomisaki and Shigaraki, Japan. A Doppler sodar measured the vertical profiles of winds in the ABL. Using the integral wavelet transform for the time series of surface wind data, the pattern of a descending high-speed structure with large vertical extent (from the surface to more than 200-m level) is depicted from the Doppler sodar data. Essentially this structure is a specific type of coherent structure that has been previously shown in experiments on turbulent boundary-layer flows. Large-scale high-speed structures in the ABL are extracted using a long time scale (240 s) for the wavelet transform. The non-dimensional interval of time between structures is evaluated as 3.0–6.2 in most cases. These structures make a large contribution to downward momentum transfer in the surface layer. Quadrant analyses of the turbulent motion measured by the sonic anemometer (20-m height) suggest that the sweep motion (high-speed downward motion) plays a substantial role in the downward momentum transfer. In general, the contribution of sweep motions to the momentum flux is nearly equal to that of ejection motions (low-speed upward motions). This contribution of sweep motions is related to the large-scale high-speed structures.

1 Introduction

Many laboratory experiments have demonstrated the existence of coherent turbulence structures in boundary-layer and pipe flows (e.g., pioneered by Kline et al. 1967; Corino and Brodkey 1969), and the results have revealed the large contributions that these structures make to the production of turbulence and turbulent transfer. Coherent structures, intermittent and spatially local flow patterns in turbulence have also been investigated in other types of flow, such as turbulent jets (Crow and Champagne 1971) and plane turbulent mixing layers (Brown and Roshko 1974). The structures appear in various forms, including streaks and vortices.

Most experiments on coherent structures were performed under conditions of low Reynolds number ($Re <10^4$) or in the near-wall region. In the case of the atmospheric boundary layer (ABL), the Reynolds number of the flow is very high ($Re \approx 10^8$) and the layer is very extensive (from the surface to $\approx$1 km in height). Therefore, the conditions are very different from those under which coherent turbulence structures were typically examined.

Large-eddy simulation (LES) models are capable of handling high Reynolds number conditions, and many studies on turbulence structures in the ABL have been performed using LES. For a neutrally stratified boundary layer, Deardorff (1972) demonstrated the existence of banded structures in the lower levels and Lin et al. (1996) studied coherent structures and flow dynamics in more detail. Although these studies have revealed many important properties of the turbulent boundary layer, the characteristics of the turbulent model for the subgrid scale are considered to influence the overall features of turbulence structures, as pointed out by Khanna and Brasseur (1998).

Field experiments in the ABL have resolved turbulence structures called microfronts (Gao et al. 1989, 1992) or gust fronts (Hayashi 1992), that structures are small-scale frontal structures containing distinct high-speed regions. Under near-neutral conditions at levels within and above a forest canopy, Gao et al. (1989) reported a flow structure consisting of a weak ejection (the region of upward motion) from the canopy top

followed by a strong sweep (the region of downward motion) into the canopy. The sweep transports dry air into the canopy and forms a microfront in the humidity field. Hayashi (1992) observed the horizontal structure of wind speed fluctuations in the surface layer with a network of anemometers, revealing a gust front at the forward edge of the high-speed region. These structures are considered to represent certain types of coherent structures in the ABL. However, as these previous experiments were conducted only in the region near the surface or plant canopy (sometimes in the roughness sublayer), the overall features of these turbulence structures in the ABL remain unclear.

Recent developments in remote sensing techniques have made it possible to visualize three-dimensional flow patterns in the ABL. Drobinski et al. (2004) showed elongated structures in the streamwise direction close to the ground with organized regions of alternating high- and low-speed fluid from observations using a high-resolution Doppler lidar. These "streaks" of higher velocity fluid were oriented parallel to the surface wind direction with a horizontal spacing of approximately 300 m in the cross-wind direction. As these observations demonstrate, there appears to be many types of coherent structures in the ABL, moreover under a variety of atmospheric stability conditions (e.g. Barthlott et al. 2007). Nevertheless, turbulence structures at higher levels in the ABL (above the surface layer) have not been investigated in detail from observational results.

Based on the results of theoretical considerations and experimental data, Hunt and Morrison (2000) proposed new concepts for the driving mechanisms and the statistics for the neutrally stratified turbulent boundary layer at very high Reynolds numbers. They suggested that the dominant mechanism is the impingement of "large-scale eddies" at the wall and the subsequent generation of rapidly increasing shear stresses within internal shear layers. These large-scale eddies are originally situated in the "middle layer" of the boundary layer, and the above process leads to the generation of small-scale turbulence and some upscale transfer of energy. Their "top-down" picture differs from the "bottom-up" instability–surface interaction mechanisms proposed in many previous studies. Following Hunt and Morrison (2000), the essential mechanisms for turbulent eddies

impinging on the wall were studied by Hunt and Carlotti (2001) using linearised rapid distortion theory. They derived predictions of the turbulence statistics in the surface layer, where eddies are affected by local shear dynamics, and in the "eddy surface layer" (lower sublayer) where quasi-independent sloping elongated eddies interact directly with the wall. Drobinski et al. (2007) presented evidence of the multiscale nature of the turbulent eddies in the neutral surface layer from the combined use of the experimental database and numerical simulations. A linear relation between the height and large-eddy scales was not applicable to the smaller eddies in the eddy surface layer, suggesting different dynamical processes driving the large and small eddies. This is consistent with the top-down picture of Hunt and Morrison (2000).

The purpose of the present study is to investigate the features of turbulence structures in the neutral ABL, especially turbulence characteristics relating to coherent structures. Specifically, the definition of the neutral boundary layer is used here for conditions in which the mechanical (shear) production of turbulent kinetic energy (TKE) is much larger than the buoyant production. The turbulence structures in such a neutral boundary layer are expected to have different aspects from those in the stable or unstable boundary layer, because the effect of buoyancy on the structures is very small. Furthermore, since most laboratory experiments were made in neutral conditions, observational results are readily compared with those experiments. In our study, field experiments for the near-neutral ABL were carried out at Shionomisaki and Shigaraki in Japan, and the characteristics of turbulence structures at these locations are examined.

2 Observations

Observations of the ABL were made at Shionomisaki in the period November to December 1998 and at Shigaraki in December 2001 to January 2002, in the late autumn and winter seasons. The Shionomisaki Wind Effect Laboratory of the Disaster Prevention Research Institute (DPRI), Kyoto University is located on a peninsula at the southernmost

part of Honshu Island (main island), Japan (33.5°N, 135.8°E) (Hayashi 1991). As the ground surface of the peninsula is roughly flat, cases where the wind direction with an overland fetch of approximately 1–2 km is suitable for observations of boundary-layer turbulence are used. This observation site is sparsely surrounded by small houses and trees. The Shigaraki MU (middle and upper atmosphere) Observatory of the Research Institute for Sustainable Humanosphere (RISH), Kyoto University is located in a gentle hilly region of Honshu Island (34.9°N, 136.1°E) (Kato et al. 1984). The surrounding terrain with some undulation is not optimal for the observation of surface-layer turbulence, but even so, the surface around the site is mostly covered by forest that continues more than approximately 2 km in all directions. Since an open field containing the antennae of the MU radar is situated near the observation point, data periods with this wind direction were not used for the analysis.

At the Shionomisaki site, a sonic anemometer-thermometer (DA-600, Kaijo Co., Tokyo, Japan) was installed at a height of 20 m on the tower of the main research office for the measurement of surface (horizontal and vertical) wind and stability. The sampling rate for this instrument was 10 Hz. Vertical profiles of winds in the ABL were measured with a Doppler sodar (AR-1000, Kaijo Co.). This has an acoustic system of phased arrays, allowing the vertical profile of three-dimensional velocity components to be acquired every 20 s with five beams (one vertical and four tilted beams) up to several hundred metres. The width of the acoustic beams is 10°, and the zenith angle of the tilted beams is 20°, while the range resolution of the measurements is approximately 30 m over a height range 40–350 m with the acoustic pulse duration of 200 ms. As a standard technique, variability due to a random error in the Doppler sodar measurements is reduced by taking mean values over a suitable averaging time (e.g. 10 min). Ito (1997) estimated the errors in wind measurements for this type of Doppler sodar; the 10-min averaged horizontal wind speeds acquired by the Doppler sodar were in good agreement with sonic anemometer measurements on a tower, with a bias of 0.14–0.28 m s^{-1} and precision of 0.47–0.52 m s^{-1}. As the present study is intended to investigate the fine structure of

turbulence, at first we use the original data. Since the Doppler sodar detects winds over a volume and at multiple points in space, direct comparison of its original data with the single point measurements from an anemometer is difficult. From a field experiment using a five-beam phased array Doppler sodar, Ito (1997) estimated the standard deviations of the errors in wind measurements to be approximately 0.41 m s^{-1} for the vertical component and 0.46 m s^{-1} for the tilted beam axis component. Since various conditions of observations increase the measurement errors, we examine the averaged values of physical quantities in the subsequent analyses.

Furthermore, at the same time as the Doppler sodar measurements, the full structure of the ABL was observed using a transportable S-band (frequency, 3.05 GHz) boundary-layer radar (Yamamoto et al. 2002) with an inter-pulse period of 50 μs. After the processing (integrations, etc.) of received signals, velocity components and the echo intensity over a height range from 200 m to approximately 5 km were acquired every 2 min.

At the Shigaraki site, two sets of cup anemometers with wind vanes (034S, Prede Co. Ltd., Tokyo, Japan) and two thermometers (PVC-04, Prede Co. Ltd.) (temperature sensor of the thermistor) were installed on poles (attached to a radio-proof fence) at heights of 4 m (3 m for the thermometer) and 17 m for the measurement of surface (horizontal) wind speed and stability. The sampling rate of the anemometers was 10 Hz, and the sampling interval of the thermometers was 10 s. A transportable Doppler sodar (KPA-1000, Kaijo Co.) was used for the observation of wind profiles in the ABL, similar to the installation at Shionomisaki. Wind measurements every 30 s with a range resolution of approximately 50 m over a height range of 50–350 m were made with an acoustic pulse duration of 300 ms. At the same time, the full structure of the ABL was observed using an L-band (frequency, 1.3575 GHz) lower troposphere radar (Hashiguchi et al. 2004), in a similar manner to the S-band boundary-layer radar at Shionomisaki.

For the data analysis, a number of discrete cases in the daytime, in which the boundary layer was near neutral, were selected from the full set of observations.

3 Results and Discussion

3.1 Fundamental Turbulence Characteristics in the Surface Layer

In this section, we examine the turbulent flows in the surface layer. As an example, a case observed at Shionomisaki from 1110 to 1448 local standard time (LST) on December 8, 1998 is considered here. The observation period of 218 min is divided into four parts, and the analysis of time-averaged statistics applies to each part. The weather in this case was cloudy with mean surface wind speeds of 7, 6, 5, and 5 m s^{-1} at 20-m height for each part. The change in wind speed over the period of this case is thus relatively small. The surface wind was northerly or north-westerly with mean directions of 340, 351, 321, and 313°. At Shionomisaki, the wind blows along the fetch over land for this wind direction.

The stability parameter for the surface layer, which is the ratio of the observation height (z) to the scaling length (L, the Obukhov length), is expressed as

$$z/L = -\frac{\left(g/\overline{\theta}\right)\left(\overline{w'\theta'}\right)_0}{u_*^3/kz},$$

(1)

where g is the acceleration due to gravity, θ is the potential temperature, w is the vertical velocity component, u_* is the friction velocity, and k is the von Karman constant ($= 0.4$). The prime denotes the fluctuation from the mean (for each part in this study), the overbar denotes the time average, and $(\ )_0$ denotes the surface value. The friction velocity is the reference velocity and is given by

$$u_* = \left(\tau_0/\rho\right)^{1/2} = \left[-\left(\overline{u'w'}\right)_0\right]^{1/2},$$

(2)

Where τ_0 is the surface shear stress, ρ is the density of air, and u is the streamwise velocity component in the horizontal plane (the velocity component in the direction of the

horizontal mean wind vector). Here, $-\rho\overline{u'w'}$ is the vertical eddy flux of streamwise momentum (Reynolds shear stress). The eddy flux, or the statistical covariance, is calculated over the averaging time of each part. The parameter z/L has essentially the same meaning as the flux Richardson number (R_f), which is the ratio of the buoyant production of turbulence to the shear production.

To be precise, the three-dimensional mean wind vector may not be situated in the horizontal plane owing to the sloping terrain. Therefore, for the analysis of data measured by the sonic anemometer at 20-m height, a coordinate transformation is applied. First, the three-dimensional mean wind direction is deduced from the original three velocity components in the instrument's reference frame. Next, the u velocity component is taken in the three-dimensional mean wind direction, and the w velocity component is taken in the direction of the upward normal to this mean wind direction. The effect of this correction is sometimes large. For example, the originally derived value of –0.30 m^2 s^{-2} for $\overline{u'w'}$ in part 1 is increased to –0.62 m^2 s^{-2}. For parts 1 to 4, the resulting friction velocity is 0.79, 0.78, 0.68, and 0.54 m s^{-1}, and the stability parameter (z/L) is –0.02, –0.02, –0.02, and 0.00, indicating near-neutral stability in the surface layer in all parts. Specifically, observational cases with the stability parameter in the range of $|z/L| < 0.1$ are considered to be in near-neutral conditions in our study.

The roughness length z_0 was calculated as 0.7, 1.2, 1.4, and 0.8 m for parts 1 to 4 from the mean value of u and the friction velocity u_* assuming the logarithmic wind profile. This value of roughness length is susceptible to the change in wind direction (different surface features) and possibly other factors.

Figure 1 shows the time series of u and w velocity components for part 1 of the observational case. Fluctuations in velocity with a wide range of time scales are apparent. The corresponding spectral characteristics of turbulence are shown in Fig. 2. Frequency (f)-weighted power spectra for the u and w components (P_u and P_w) for each part are normalized with respect to u_*^2 and shown as a function of non-dimensional frequency n ($= fz/\overline{u}$). Further, these spectra are averaged over parts 1 to 4. Finally, the large scatter in

spectral estimates is reduced by smoothing with a frequency window after Kaimal and Finnigan (1994). In Fig. 2, broad spectral peaks are observed near a non-dimensional frequency of 0.02 for the u component and 0.4 for the w component. As the non-dimensional frequency is the ratio of height z to wavelength λ $(=\bar{u}/f)$, these peak locations correspond to spatial scales of 1000 and 50 m.

To investigate the most effective scale of turbulence in the downward transfer of momentum towards the surface, the cospectrum of the streamwise and vertical velocity components (u and w) is analyzed. In this case, the cospectrum represents the contribution of eddies on each scale with respect to the mean value of $u'w'$ (Reynolds shear stress). The u and w velocity components are taken in the manner described above. Negative values of the cospectrum imply a downward momentum flux. Figure 3 shows the averaged cospectrum ($C_{uw}(f)$) over parts 1 to 4 after normalization by u_*^2 on the scale of non-dimensional frequency. Large scatter of cospectral estimates is reduced in the same way as for the power spectra. This figure shows that the eddies exerting the largest effect on the momentum flux have a non-dimensional frequency scale in the range of approximately 0.02–0.1. This range corresponds to 200–1000 m on the spatial scale.

The features outlined above are similar to those reported in previous studies on surface-layer turbulence under neutral stability conditions (e.g. Kaimal and Finnigan 1994). In subsequent sections, we describe the results for December 8, 1998 at Shionomisaki as a typical case. Other observational cases at Shionomisaki and Shigaraki are used in order to examine the more general characteristics.

3.2 Turbulence Structures in the Atmospheric Boundary Layer

The wind structure of the ABL was observed using the Doppler sodar, and we show the case examined in the previous section, which was observed at Shionomisaki on December 8, 1998. Figure 4 shows the mean vertical profiles of horizontal wind speed (U) and wind direction for part 1 up to a height of 350 m. These profiles reveal small changes in wind

speed above 100 m and in wind direction over the entire measured range. The wind speed varies approximately logarithmically with height at levels below 100 m, which probably corresponds to the surface layer. On the other hand, the depth of the ABL can be estimated from the abrupt decrease in echo intensity of the S-band boundary-layer radar at the top of the layer, since atmospheric turbulence is the primary cause of the echo and its intensity is usually weak above the ABL. In this case, the estimated average depth of the ABL is 1.1 km. Therefore, the Doppler sodar measures wind profiles in the lower part of the ABL. On the occasion of this observation, wind measurements using the S-band radar were insufficient for the construction of vertical profiles.

Figure 5 shows the time–height cross-section of the streamwise velocity component in the horizontal plane (u), which is constructed from the original Doppler sodar data for part 1 of this case. The time series of the streamwise velocity component in the horizontal plane measured by the sonic anemometer is also shown in the lower part of this figure. Because of the restricted accuracy of the Doppler sodar, the analysis procedure for the three-dimensional mean wind vector was not applied here. Furthermore, streamwise velocity components at all measurement levels of the Doppler sodar are taken in the same direction as the mean surface wind from the sonic anemometer measurements. Regions of high and low velocity with roughly estimated time scales of 100–300 s are recognized in the time–height cross-section of the Doppler sodar data. These large-scale regions are also rather extensive in the vertical direction. When the large-scale regions of high velocity extend down to levels lower than 100 m, large-scale high-speed wind events are also likely to happen in the time series of surface-layer turbulence. The ellipses with dashed lines in Fig. 5 show the typical large-scale regions of high velocity. At the height of 200 m, the maximum value of the u velocity component reaches 24 m s^{-1} in the second ellipse ($\bar{u} = 11$ m s^{-1} at this height). The corresponding peak value of u in the surface layer is 12.6 m s^{-1} ($\bar{u} = 6.4$ m s^{-1}). In the following analysis, these large-scale high-speed structures are examined in more detail. As these structures appear intermittently, the contribution of such features to the averaged spectrum may not be large. With regard to

this point, the spectral peak in Fig. 2 for the *u* velocity component corresponds to a time scale of approximately 200 s.

Specific structures are extracted from the turbulence data by applying an integral wavelet transform to the measured time series $x(t)$. The wavelet transform (wavelet coefficient) $T(a, b)$ with a scale parameter a and a translation parameter b is defined as

$$T(a,b) = \left(\frac{1}{a}\right)\int_{-\infty}^{+\infty}\Psi\left(\frac{t-b}{a}\right)^{*}x(t)dt, \tag{3}$$

where $(1/a)\Psi((t-b)/a)$ is a wavelet, and $\Psi(t)$ is an analyzing wavelet (mother wavelet). The asterisk denotes the complex conjugate of the function. The scale parameter a affects the size and amplitude of the wavelet, and the translation parameter b sets the location of the wavelet. The discrete form of Eq. (3) is applied to the present measurements.

It is clear from Eq. (3) that the value of the wavelet coefficient is also dependent on the shape of the analyzing wavelet. From the various analyzing wavelets proposed previously, the "Mexican Hat" wavelet function is employed here, given by

$$\Psi(t) = (1 - t^2)\exp(-t^2/2), \tag{4}$$

a function that is well localized in both time and frequency, with a smooth and symmetrical shape. It has been used in studies on turbulence (e.g. Gao and Li 1993; Chen and Hu 2003). As the scale parameter a is the half-width of the positive part of this wavelet, the time scale defined by the value of $2a$ is used for sorting structures of different scales. In order to examine the energy distribution for the scale, the wavelet variance spectrum $W(a)$ (e.g. Collineau and Brunet 1993; Thomas and Foken 2007) is calculated as follows:

$$W(a) = \int_{-\infty}^{+\infty} |T(a,b)|^2 db.$$ (5)

High-speed wind events with large time scales are identified by applying the wavelet transform to surface-layer turbulence data measured by the sonic anemometer. For the wavelet transform, we calculate the fluctuation from the mean for the streamwise velocity component in the horizontal plane (u') and normalize the result with respect to its standard deviation (σ_u) in each part, taking into consideration the gradual change in mean wind speed and the magnitude of fluctuations during one case (period of 218 min). As the wavelet variance spectrum does not show a distinctive peak at the larger time scale (>100 s), a fixed time scale of 160 s ($a = 80$ s) is used for the purpose of detecting large structures such as high-speed wind events indicated in Fig. 5. Conversion of the time scale into the spatial scale using Taylor's frozen turbulence hypothesis yields a scale of approximately 800 m from the mean value of u in this case. This spatial scale is near to the average depth of the ABL. In this connection, the time scale used here is larger than the dominant (most probable) or characteristic (mean) value of structure duration in previous studies (Barthlott et al. 2007; Thomas and Foken 2007).

From the series of wavelet coefficients on the translation parameter b, we pick up high-speed wind events with relative maxima exceeding a threshold value. This threshold value has an effect on the number of detected events and the resulting averaged pattern of the structure. Moreover, the lower threshold leads to the large variation in wind fields between the events. In order to capture a distinctive structure with a sufficient number of events, a certain threshold value was applied (2.8 to this case). Using data from the Doppler sodar, a conditionally averaged wind pattern is then constructed from six detected events in this observational case and depicted on a time–height cross-section (zero is the time of the events) (Fig. 6). The fluctuations of streamwise (u) and vertical (w) velocity components, normalized with respect to their standard deviations (σ_u and σ_w), are used for averaging. In Fig. 6, normalized u' values are indicated by contours, and normalized w' values are denoted by arrows. In addition, time progresses in the direction

from the right to the left. In regard to the time scale of the wavelet, an averaged wind pattern similar to that in Fig. 6 can be constructed with a time scale larger than the selected one. However, the wind pattern becomes unclear (a broad region of high velocity), probably because the widened peak of the wavelet with a larger time scale makes the determination of the central time of events ambiguous.

A descending high-speed structure with the estimated time scale of 50–100 s is recognized from the averaged wind pattern of Fig. 6, the central part (maximum normalized u' value) of which is located at the height of 200 m and near the time of 30 s prior to the time of the events. The maximum value of u'/σ_u reaches 1.6, while the averaged values of $\bar{u}$ and σ_u over parts 1 to 4 are 8.1 and 3.0 m s^{-1} at 200-m height. In advance of the high-speed structure, a low-speed region ascending slightly at the time near 140 s prior to the event time is also revealed. The upper portion of the high-speed structure appears a little earlier than its lower portion. When the temporal variation is converted into the spatial distribution, this pattern shows a high-speed structure (spatial scale of 400–800 m from $\bar{u}$ at 200-m height) tilting toward the downwind direction. From the position of maximum normalized u' relative to the location of the detected events at 20-m height, the tilt angle is estimated to be 53° from the vertical. Compared to the depth of the ABL (1100 m on average), this structure has fairly large scales in the vertical and streamwise directions. Considering also the vertical profiles of wind direction (e.g. Fig. 4), the deviation of the structure from the vertical plane toward the lateral direction is not large.

This pattern is similar to the structures reported previously based on observations (Gao et al. 1989) and numerical experiments using LES (Su et al. 1998; Watanabe 2004) for plant canopies. These studies revealed microfrontal structures of scalar concentration and ejection-sweep structures of velocity. Using the data acquired by low-level aircraft flights, Mahrt (1991) reported that horizontal convergence at the microfront can be interpreted as the result of descending wind gusts impinging on slower moving air rising from the surface. Compared to the foregoing observations (up to approximately twice the

forest height in Gao et al. 1989), the present Doppler sodar observations make it possible to investigate the structures over a wide height range. Although the mechanism of generation of these large-scale high-speed structures cannot be clarified in our study, the downward movement of the high-speed structure in a real sense, the maximum w value of -2.6 m s^{-1}, suggests that the structure has arrived from considerably higher levels in the ABL.

Nine other cases in which near-neutral stability conditions prevailed were also analyzed in the present study (10 cases in total). The conditions of wind speed at the height of 20 m (Shionomisaki) or 17 m (Shigaraki), surface shear stress, stability in the surface layer, and depth of the ABL for these cases (including the case on December 8, 1998 at Shionomisaki) are listed in Table 1. The average ABL depth was estimated on the basis of echo intensities by the S-band boundary-layer radar (Shionomisaki) or the lower troposphere radar (Shigaraki). At Shionomisaki, for the case on November 17, 1998, S-band radar observations were not made. Observations are referred to as case A1–A5 (at Shionomisaki) and B1–B5 (at Shigaraki), with conditions that lie in the range 4–8 m s^{-1} for surface wind speed and 0.5–1.0 m s^{-1} for friction velocity, which is favourable for the comparative analysis. Calculated values of roughness length are in the range of 0.2–1.4 m in the cases at Shionomisaki and 0.5–0.9 m in the cases at Shigaraki, depending on the wind direction and possibly other conditions. Among the cases at Shionomisaki when S-band BLR observations were made, case A4 (on December 8, 1998) examined so far has a minimum average value of $|z/L|$ (closest to neutral conditions). In all cases, observations exhibit similar wind patterns according to the present analytical process, revealing large-scale high-speed structures. Thus, it appears likely that the turbulence structure depicted in Fig. 6 is a common feature of the near-neutral ABL.

3.3 Overall Features of Turbulence Structures and Contribution to Momentum Transfer

The overall appearance of turbulence structures in the ABL is investigated in this section.

As a simple method, regions of turbulence structures in the time–height cross-section (e.g. Fig. 5) can be delineated by applying the integral wavelet transform to the data series at each level observed by the Doppler sodar. Precise measurements of surface wind by the anemometer at a high sampling rate are also applied to determine the periods of turbulence structures. Large-scale structures are extracted using a rather long time scale of 240 s (a = 120 s) for the wavelet transform. This time scale is larger than that in the previous analyses (Section 3.2), because the lower troposphere radar at Shigaraki can acquire wind profiles only every 2 min (the minimal value of the scale parameter a is 120 s). A threshold value of 0.5 for the wavelet coefficient is employed in order to extract distinct regions of high-speed structures for a sufficient number of times (for the subsequent analysis) during the observation period. Changing the threshold value alters the total number and duration of the determined regions or periods of high-speed structures. This was examined for the sonic anemometer data in the case of December 8, 1998 at Shionomisaki (case A4). Figure 7 illustrates the variation of the total number of high-speed structures in this case with the threshold value for wavelet coefficients. Above the threshold value near 0.5, the total number of structures decreases rapidly. For further high threshold values above the value near 1.2, a small number of structures (strong events) remain. Considering this tendency, the threshold value was selected. Even so, it seems that the criterion to extract the turbulence structures inevitably is arbitrary.

Figure 8 shows the time–height cross-section of wavelet coefficients for the streamwise velocity component in the horizontal plane (u) observed by the Doppler sodar (upper figure) and the time series of wavelet coefficients for the same velocity component measured by the sonic anemometer at 20-m height (lower figure) for the case on December 8, 1998 at Shionomisaki. Fluctuations normalized with respect to the standard deviations in each part are used for this analysis of the wavelet transform. In the upper figure, areas of light tone denote regions in which the wavelet coefficient for the Doppler sodar data is larger than the threshold value (0.5), and bold bars show periods during which the wavelet coefficient for the sonic anemometer data is larger than the threshold

value (0.5). The areas of light tone in the time–height cross-section, corresponding to high-speed structures, clearly show the wide extent in the vertical direction. In addition, the periods of high-speed structures in the surface layer measured by the sonic anemometer, which is indicated by the bold bars, have a significant correlation with the structures in the higher levels observed by the Doppler sodar.

The intermittent occurrence of these large-scale structures (with large vertical extent) resembles the "bursting phenomenon" investigated in many experiments on the turbulent boundary layer (e.g. Kline et al. 1967). The turbulent burst is a sequence of events involving lift-up, oscillation, and break-up (sometimes only the break-up and related phenomena are referred to as the burst) of a low-speed streak originally located in the near-wall region of turbulent flows. The mean interval of time between bursts (T_B) or the bursting frequency for its inverse is an important parameter associated with the bursting process. Based on various laboratory experiments of their own and of other investigations, Rao et al. (1971) obtained a value near 5 for the non-dimensional interval of time between bursts or normalized burst rate ($U_\infty T_B /\delta$) with scaling on the outer region variables, where U_∞ is the free-stream velocity and δ is the boundary-layer thickness. In their interpretation, the bursts are separated on average by a distance L ($\sim U_\infty T_B$) of the order of several boundary-layer thicknesses. On this subject, as Sabot and Comte-Bellot (1976) pointed out, weaker bursts would be included and the mean interval of time between bursts would decrease if the criterion for counting the bursts were made less severe. From the experimental data obtained in an open-channel flow, Komori et al. (1989) also considered the effect of the threshold level and averaging time on the bursting frequency detected by the variable interval time-averaging technique.

In the present case, 18 periods of high-speed structures during the full observational case (202 min for the analysis) were detected using the adopted threshold value of 0.5 from the wavelet coefficients for the u velocity component obtained by the sonic anemometer. The mean interval of time between the structures (T_S) is 670 s, corresponding to a spatial scale of 3,500 m. In this connection, the mean duration of the

structures is 170 s. Therefore, the time fraction of the total period is evaluated as 25%. In regard to the number of structures, Barthlott et al. (2007) observed on average between 7 and 11 coherent structures every 30 min in the surface layer. It is likely that their method using the most representative scale from the wavelet variance spectrum detects small-scale structures as compared to the present analysis, as was pointed out in the previous section.

In analogy to the bursting phenomenon, the non-dimensional interval of time between structures (T_N) is evaluated as follows:

$$T_N = U_\infty T_S /\delta = 3.3, \tag{6}$$

where the mean value of the u velocity component at the top level measured correctly by the Doppler sodar (5.4 m s^{-1} at 350 m in this case) is used for the free-stream velocity (U_∞) and the value of estimated average ABL depth (1100 m) is used for δ. By an argument similar to that for the turbulent bursts, changing the threshold value affects the above evaluation for the intermittency of turbulence structures. For example, the use of a threshold value of 0.3 reduces the non-dimensional interval of time between structures (T_N) to a value of 2.8.

The same analytical procedure is applied to the case observed at Shigaraki, where the lower troposphere radar is also available for the measurement of wind profiles. As a typical example, the observational case of December 10, 2001 (case B1) is analyzed, when the average value of $|z/L|$ is the lowest (closest to neutral) of all cases at Shigaraki. Originally, this radar measures the zonal and meridional components of horizontal wind. When one of the velocity components cannot be measured, as is often the case under the present observational conditions, the streamwise velocity component (u) becomes indeterminant. As the mean surface wind direction was close to north on December 10, 2001, the southward component of wind (from the meridional component) was used as an approximate estimate for the streamwise velocity component. At times when this

component was not obtained, linear interpolation was applied to fill up the data series.

Figure 9 shows the time–height cross-sections of wavelet coefficients for the southward component of wind observed by the lower troposphere radar (upper figure) and for the u velocity component observed by the Doppler sodar (middle figure), and the time series of wavelet coefficients for the u velocity component measured by the cup anemometer with the wind vane at 17-m height (lower figure). As with Fig. 8, areas of light tone in the upper and middle figures denote regions in which the wavelet coefficient is larger than the threshold value (0.5), and bold bars in the middle figure show periods during which the wavelet coefficient for the anemometer data is larger than the threshold value (0.5). The average depth of the ABL was estimated to be 1.0 km from the radar echo intensities. As shown in Fig. 9, the lower troposphere radar can detect wind profiles up to a level above the top of the ABL, and in the upper part of the ABL this radar can resolve turbulence structures similar to those observed by the Doppler sodar. Owing to the intervening layer, which could not be observed by the Doppler sodar or radar, the relationship between the turbulence structures in the two observed layers is unclear.

For this case at Shigaraki, the non-dimensional interval of time between high-speed structures determined by the above method is larger than that for case A4 (at Shionomisaki). With the threshold value of 0.5 applied to the wavelet coefficients for the anemometer data, we evaluate $T_N = 6.9$. This result may be affected by the terrain around the site of Shigaraki. When the wavelet coefficients for the u velocity component at the second measurement level of the Doppler sodar (75 m) is used for detecting the structures, the value of T_N slightly decreases to 6.2.

The values of the non-dimensional interval of time between high-speed structures in all cases are shown in Table 2. Structures are extracted from the wavelet coefficients for the u velocity component at the level of 40 m (Shionomisaki) or 75 m (Shigaraki) observed by the Doppler sodar. We used the same threshold value of 0.5 as in the above-mentioned cases. Also in Table 2, the mean distances between structures, which were converted from the mean interval of time by using the mean value of u at the same

measurement level, are listed. In the case of no measurement for the depth of the ABL (case A1), only the mean distance was evaluated.

Obtained values in the range of 3.0–6.2 for the non-dimensional interval of time between high-speed structures, except for the rather high value in case A3, almost coincide with the general value of the normalized burst rate. Although their evolution processes may be different from each other, resultant structures have similar appearances. Spatial structures of turbulent bursts and the evolution of their features with time have been precisely investigated in laboratory experiments. On the other hand, the three-dimensional spatial structure and temporal evolution of the high-speed structures in the ABL have not been observed to date. As for the mean distances between high-speed structures, a small change in the range of 3,800–5,400 m is indicated in Table 2. This implies that a common process is present in the formation of these structures.

For the next step of the analysis, the contribution of large-scale high-speed structures to momentum transfer is examined. Since the large sampling interval of the Doppler sodar is insufficient to detect all dominant eddies (e.g. frequency scale of approximately 0.005–0.026 s^{-1} from the cospectral analysis for case A4), the sonic anemometer measurements at Shionomisaki (20-m height) are used to investigate the contribution of these structures in the surface layer. For the evaluation of the relative importance to momentum transfer, the average value of instantaneous $u'w'$ in the large-scale high-speed structures decided as above is compared with the overall average value of $u'w'$ for the entire analyzed period. This ratio is the same as the transport efficiency of structures, which was introduced by Barthlott et al. (2007). For the $u'w'$ values, the u and w velocity components are taken in the same manner as in Section 3.1. The result for the case on December 8, 1998 at Shionomisaki (case A4) is a value of 1.35, revealing that large-scale high-speed structures make a large contribution to momentum transfer. In this case, the high-speed structures determined by the sonic anemometer data, which cover 25% of the entire analyzed period, transfer 34% of the momentum at this level (20 m).

The same analyses of the efficiency of large-scale high-speed structures for

momentum transfer were made for other observational cases at Shionomisaki. The ratios of the average $u'w'$ values in the structures to the overall average values at 20-m height in the surface layer are 1.22 (case A1), 1.36 (A2), 1.22 (A3), and 1.15 (A5), illustrating the relative importance of high-speed structures to momentum transfer. Observational results (limited to the surface layer in this study) suggest the strong effect of large-scale high-speed structures on the downward transfer of momentum in the ABL.

3.4 Ejection and Sweep Motions

Turbulent motion can be classified into four quadrants on the u', w' plane as follows:

$$u' \geq 0, \ w' \geq 0 \ (\text{outward interaction}), \tag{7a}$$

$$u' < 0, \ w' \geq 0 \ (\text{ejection}), \tag{7b}$$

$$u' < 0, \ w' < 0 \ (\text{inward interaction}), \tag{7c}$$

$$u' \geq 0, \ w' < 0 \ (\text{sweep}). \tag{7d}$$

In these quadrants, ejection and sweep motions contribute to the downward transfer of momentum ($u'w' < 0$). The ejection motion is a low-speed upward turbulent motion and the sweep motion is a high-speed downward turbulent motion. In this connection, the flux fraction is the relative contribution of the motion in each quadrant to the momentum flux (Reynolds shear stress) by all motions. For the velocity fluctuations measured by the sonic anemometer at 20-m height on December 8, 1998 at Shionomisaki (case A4), the flux fraction due to sweep motions (0.93) is slightly larger than that due to ejection motions (0.84). The flux fractions are compared in all cases at Shionomisaki, and the ratios of the fractions due to sweep motions to those due to ejection motions are 0.90, 0.97, 0.85, 1.10, and 0.83 for cases A1–A5. In general, nearly equal contributions are seen.

In the present observations, the contribution of sweep motions is likely related to the large-scale high-speed structures, which have large effects on the downward momentum

transfer and implicitly downward movements in the ABL. Indeed, downward vertical velocities averaged for large-scale high-speed structures for the case on December 8, 1998 at Shionomisaki (case A4) reach 0.2 m s^{-1} at 20-m height measured by the sonic anemometer and 0.1–0.4 m s^{-1} at each level (40–200 m) due to the Doppler sodar measurements.

The relationship of sweep motions to the large-scale high-speed structures is specifically examined for case A4. Figure 10 shows the time–height cross-section of the streamwise velocity component in the horizontal plane (u) observed by the Doppler sodar (upper figure) and the time series of the same velocity component measured by the sonic anemometer at 20-m height (middle figure) from 1132 to 1159 LST (in part 1 of the case). Instantaneous $u'w'$ values at the times of ejection and sweep motions measured by the sonic anemometer are also shown (lower figures). The ellipses with dashed lines in the time–height cross-section show the typical large-scale regions of high velocity. In addition, the bold bars below the time series of u measured by the sonic anemometer show periods of high-speed structures, during which the wavelet coefficient for the sonic anemometer data is larger than the threshold value (0.5). This figure demonstrates the correspondence between the high-speed structures extending from higher levels and the periods when the sweep motion prevails in the surface layer. In this case, the accumulated $u'w'$ value for the sweep motions in the surface layer (20-m height) during the high-speed structures (a time fraction of 25%) amounts to 53% of the momentum flux carried by the sweep motions. The efficiency factor of the high-speed structures for the momentum flux by the sweep motions, which is obtained as the ratio of the above flux fraction to the time fraction, is 2.1 for this case. The values of the efficiency factor for all cases at Shionomisaki are shown in Table 3. When the periods of high-speed structures are determined by the sonic anemometer data as in the above example, all cases provide similar efficiency factors in the range of 1.8–2.3. This result indicates that large-scale high-speed structures have a large impact on turbulence in the surface layer. These structures induce much transfer of momentum by the sweep motions. When the

Doppler sodar data (40-m level) are used to determine the periods of turbulence structures, efficiency factors become lower (the right-most column in Table 3) owing to the distance between the two levels. Even so, large-scale high-speed structures at higher levels, possibly extending from the middle layer of the ABL (see the time–height cross-section in Fig. 8), induce a great deal of sweep motion in the surface layer.

4 Concluding remarks

We studied high Reynolds number flow in the near-neutral ABL to clarify features of coherent turbulence structures and the related processes for momentum transfer. By the method of event detection using an integral wavelet transform, a descending high-speed structure was revealed by Doppler sodar. This structure is essentially a specific type of coherent structure that has been previously shown in experiments on turbulent boundary-layer flow. In advance of the high-speed structure, an ascending low-speed region was also revealed. These form an ejection-sweep structure, consistent with the results of previous field and numerical experiments.

The regions of large-scale high-speed structures in the time–height cross-section using Doppler sodar observations were identified with the integral wavelet transform. For the wavelet, we employed a rather long time scale of 240 s, a scale that is comparable to the depth of the ABL when converted into the spatial scale. As pointed out regarding the non-dimensional interval of time between structures, some features of such large-scale high-speed structures may be similar to those of turbulent bursts. In all cases observed using the sonic anemometer in the surface layer (at Shionomisaki), the average values of $u'w'$ in the high-speed structures are larger than the overall average values. For the example case of December 8, 1998 at Shionomisaki, this ratio (transport efficiency) reaches a value of 1.35. These large-scale high-speed structures thus have a large effect on the downward transfer of momentum.

Quadrant analyses of turbulent motion in the surface layer indicate the substantial role

of sweep motions in downward momentum transfer. Instantaneous $u'w'$ values also demonstrate the large impact of large-scale high-speed structures on the turbulent motion of sweeps. It is important to examine precisely the momentum transfer process in the surface layer, especially connected with the intrusion of fast-moving regions upon the surface. The large-scale high-speed structures observed in the present study likely correspond to the "large-scale eddies" suggested by Hunt and Morrison (2000). A typical high-speed structure revealed in our study has a fairly large horizontal scale (400–800 m) compared to the depth of the ABL (1100 m). Furthermore, downward movement of the high-speed structures yields a region of large wind shear and high Reynolds shear stress.

Foster et al. (2006) examined the near-surface flow in a well-resolved neutrally-stratified large-eddy simulation of the ABL, and showed that ejection and sweep events are intimately related to the streamwise near-surface streaks of high-speed and low-speed flows. Although the structures of streaks could not be identified by our profile observations, there is a possibility that the large-scale high-speed structures examined in our study have some connection with the streaks. So far, the features of "low-speed" structures and their effect on momentum transfer have not been mentioned in the present investigation. Although some analyses of such structures have not indicated the meaningful importance to momentum transfer, the precise study of the low-speed structures connected with the ejection motion is also an important subject.

Observational cases at two places were examined in our study, and further observations including those at other sites and in different conditions are considered necessary in order to refine our findings. Three-dimensional spatial structures of turbulence and the evolution of these structures are also of interest, and their study will require numerical experiments or fast-scan observations with remote sensing instruments.

References

Barthlott C, Drobinski P, Fesquet C, Dubos T, Pietras C (2007) Long-term study of coherent structures in the atmospheric surface layer. Boundary-Layer Meteorol 125:1–24

Brown GL, Roshko A (1974) On density effects and large structure in turbulent mixing layers. J Fluid Mech 64:775–816

Chen J, Hu F (2003) Coherent structures detected in atmospheric boundary-layer turbulence using wavelet transforms at Huaihe River basin, China. Boundary-Layer Meteorol 107:429–444

Collineau S, Brunet Y (1993) Detection of turbulent coherent motions in a forest canopy part I: wavelet analysis. Boundary-Layer Meteorol 65:357–379

Corino ER, Brodkey RS (1969) A visual investigation of the wall region in turbulent flow. J Fluid Mech 37:1–30

Crow SC, Champagne FH (1971) Orderly structure in jet turbulence. J Fluid Mech 48:547–591

Deardorff JW (1972) Numerical investigation of neutral and unstable planetary boundary layers. J Atmos Sci 29:91–115

Drobinski P, Carlotti P, Newsom RK, Banta RM, Foster RC, Redelsperger J-L (2004) The structure of the near-neutral atmospheric surface layer. J Atmos Sci 61:699-714

Drobinski P, Carlotti P, Redelsperger J-L, Banta RM, Masson V, Newsom RK (2007) Numerical and experimental investigation of the neutral atmospheric surface layer. J Atmos Sci 64:137-156

Foster RC, Vianey F, Drobinski P, Carlotti P (2006) Near-surface coherent structures and the vertical momentum flux in a large-eddy simulation of the neutrally-stratified boundary layer. Boundary-Layer Meteorol 120:229-255

Gao W, Li BL (1993) Wavelet analysis of coherent structures at the atmosphere–forest interface. J Appl Meteorol 32:1717–1725

Gao W, Shaw RH, Paw U KT (1989) Observation of organized structure in turbulent flow within and above a forest canopy. Boundary-Layer Meteorol 47:349–377

Gao W, Shaw RH, Paw U KT (1992) Conditional analysis of temperature and humidity microfronts and ejection/sweep motions within and above a deciduous forest. Boundary-Layer Meteorol 59:35–57

Hashiguchi H, Fukao S, Moritani Y, Wakayama T, Watanabe S (2004) A Lower Troposphere Radar: 1.3-GHz active phased-array type wind profiler with RASS. J Meteorol Soc Jpn 82:915–931

Hayashi T (1991) The horizontal distribution of space correlation coefficients of wind fluctuations in the atmospheric surface layer. Boundary-Layer Meteorol 55:125–140

Hayashi T (1992) Gust and downward momentum transport in the atmospheric surface layer. Boundary-Layer Meteorol 58:33–49

Hunt JCR, Carlotti P (2001) Statistical structure at the wall of the high Reynolds number turbulent boundary layer. Flow Turbul Combust 66:453-475

Hunt JCR, Morrison JF (2000) Eddy structure in turbulent boundary layers. Eur J Mech B 19:673–694

Ito Y (1997) Errors in wind measurements estimated by five-beam phased array Doppler sodar. J Atmos Ocean Technol 14:792–801

Kaimal JC, Finnigan JJ (1994) Atmospheric boundary layer flows. Oxford University Press, New York, 289 pp

Kato S, Ogawa T, Tsuda T, Sato T, Kimura I, Fukao S (1984) The middle and upper atmosphere radar: first results using a partial system. Radio Sci 19:1475-1484

Khanna S, Brasseur JG (1998) Three-dimensional buoyancy- and shear-induced local structure of the atmospheric boundary layer. J Atmos Sci 55:710–743

Kline SJ, Reynolds WC, Schraub FA, Runstadler PW (1967) The structure of turbulent boundary layers. J Fluid Mech 30:741–773

Komori S, Murakami Y, Ueda H (1989) The relationship between surface-renewal and bursting motions in an open-channel flow. J Fluid Mech 203:103–123

Lin C-L, McWilliams JC, Moeng C-H, Sullivan PP (1996) Coherent structures and dynamics in a neutrally stratified planetary boundary layer flow. Phys Fluids 8:2626–2639

Mahrt L (1991) Eddy asymmetry in the sheared heated boundary layer. J Atmos Sci 48:472–492

Rao KN, Narasimha R, Badri Narayanan MA (1971) The 'bursting' phenomenon in a turbulent boundary layer. J Fluid Mech 48:339–352

Sabot J, Comte-Bellot G (1976) Intermittency of coherent structures in the core region of fully developed turbulent pipe flow. J Fluid Mech 74:767–796

Su H-B, Shaw RH, Paw U KT, Moeng C-H, Sullivan PP (1998) Turbulent statistics of neutrally stratified flow within and above a sparse forest from large-eddy simulation and field

observations. Boundary-Layer Meteorol 88:363–397

Thomas C, Foken T (2007) Organised motion in a tall spruce canopy: temporal scales, structure spacing and terrain effects. Boundary-Layer Meteorol 122:123–147

Watanabe T (2004) Large-eddy simulation of coherent turbulence structures associated with scalar ramps over plant canopies. Boundary-Layer Meteorol 112:307–341

Yamamoto M, Hashiguchi H, Fukao S, Shibano Y, Imai K (2002) Development of a transportable 3-GHz wind profiler for wind and precipitation studies. J Meteorol Soc Jpn 80:273–283

Table 1 Surface wind speed at 20-m height (Shionomisaki) or 17 m (Shigaraki), friction velocity (u_*), stability parameter (z/L), and ABL depth for the observational cases examined in the present analysis

Site	Date	Time (LST)	Part no.	Surface wind speed (m s^{-1})	u_* (m s^{-1})	z/L	ABL depth (km)	Case no.
Shionomisaki	17 Nov. 1998	1230–1608	1	7.3	0.83	–0.02	–	A1
			2	7.6	0.83	0.00		
			3	7.0	0.77	0.01		
			4	7.8	0.82	0.01		
	21 Nov. 1998	1230–1608	1	7.9	0.93	–0.07	1.5	A2
			2	7.3	0.84	–0.06		
			3	6.9	0.77	–0.04		
			4	6.2	0.71	–0.03		
	4 Dec. 1998	1000–1338	1	7.0	0.59	0.00	0.9	A3
			2	7.0	0.64	–0.03		
			3	7.2	0.65	–0.03		
			4	7.6	0.71	–0.03		
	8 Dec. 1998	1110–1448	1	6.8	0.79	–0.02	1.1	A4
			2	5.8	0.78	–0.02		
			3	4.9	0.68	–0.02		
			4	4.6	0.54	0.00		
	9 Dec. 1998	1340–1718	1	5.3	0.66	–0.09	1.2	A5
			2	5.6	0.56	–0.07		
			3	6.0	0.54	–0.04		
			4	4.8	0.51	0.01		
Shigaraki	10 Dec. 2001	0900–1238	1	6.0	0.73	–0.02	1.0	B1
			2	6.7	0.84	–0.02		
			3	7.0	0.80	–0.02		
			4	7.2	0.92	–0.02		
	15 Dec. 2001	0830–1208	1	5.5	0.64	–0.04	1.7	B2
			2	5.4	0.65	–0.03		
			3	7.0	0.83	–0.02		
			4	7.1	0.85	–0.02		
	16 Dec. 2001	0830–1208	1	4.7	0.63	–0.04	1.0	B3
			2	4.7	0.58	–0.06		
			3	5.8	0.79	–0.03		
			4	4.8	0.65	–0.08		
	9 Jan. 2002	0900–1238	1	6.0	0.82	–0.03	1.4	B4
			2	6.0	0.78	–0.03		
			3	5.6	0.76	–0.05		
			4	5.7	0.71	–0.05		
	30 Jan. 2002	0920–1258	1	5.4	0.68	–0.05	1.2	B5
			2	5.4	0.69	–0.05		
			3	6.5	0.78	–0.04		
			4	6.5	0.73	–0.05		

Table 2 Mean distance and non-dimensional interval of time between high-speed structures

Site	Date	Case no.	Mean distance between structures (m)	Non-dimensional interval of time between structures
Shionomisaki	17 Nov. 1998	A1	5200	–
	21 Nov. 1998	A2	4900	3.0
	4 Dec. 1998	A3	4500	8.7
	8 Dec. 1998	A4	3800	3.5
	9 Dec. 1998	A5	4700	4.5
Shigaraki	10 Dec. 2001	B1	5400	6.2
	15 Dec. 2001	B2	5100	4.0
	16 Dec. 2001	B3	3900	5.5
	9 Jan. 2002	B4	5100	4.9
	30 Jan. 2002	B5	4300	4.4

Table 3 Efficiency factors of the high-speed structures for the momentum flux by the sweep motions, where the structures are determined by the sonic anemometer data (20-m height) or the Doppler sodar data (40-m level)

Site	Date	Case no.	Efficiency factor	
			Structures by sonic anemometer (20 m)	Structures by Doppler sodar (40 m)
	17 Nov. 1998	A1	2.1	1.5
	21 Nov. 1998	A2	2.3	1.6
Shionomisaki	4 Dec. 1998	A3	1.8	1.2
	8 Dec. 1998	A4	2.1	1.7
	9 Dec. 1998	A5	2.0	1.4
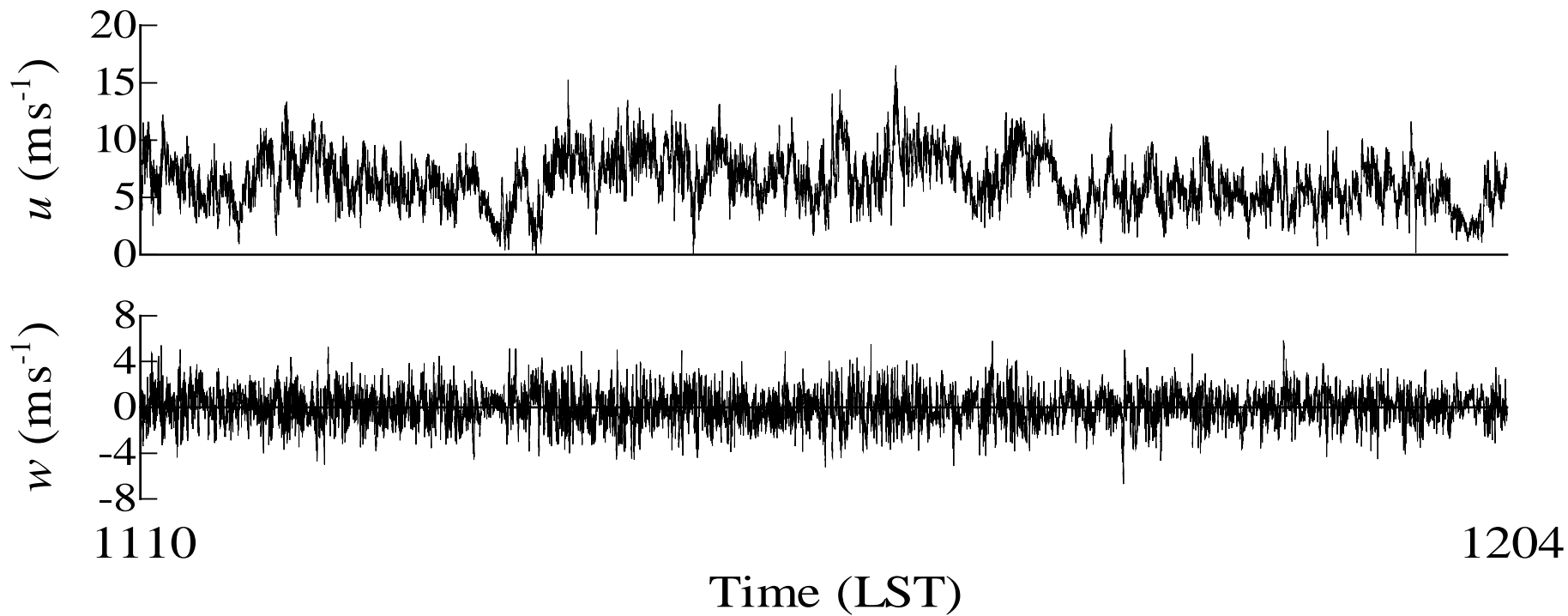
Fig. 1 Time series of u and w velocity components measured by the sonic anemometer for part 1 of the observational case on December 8, 1998 at Shionomisaki
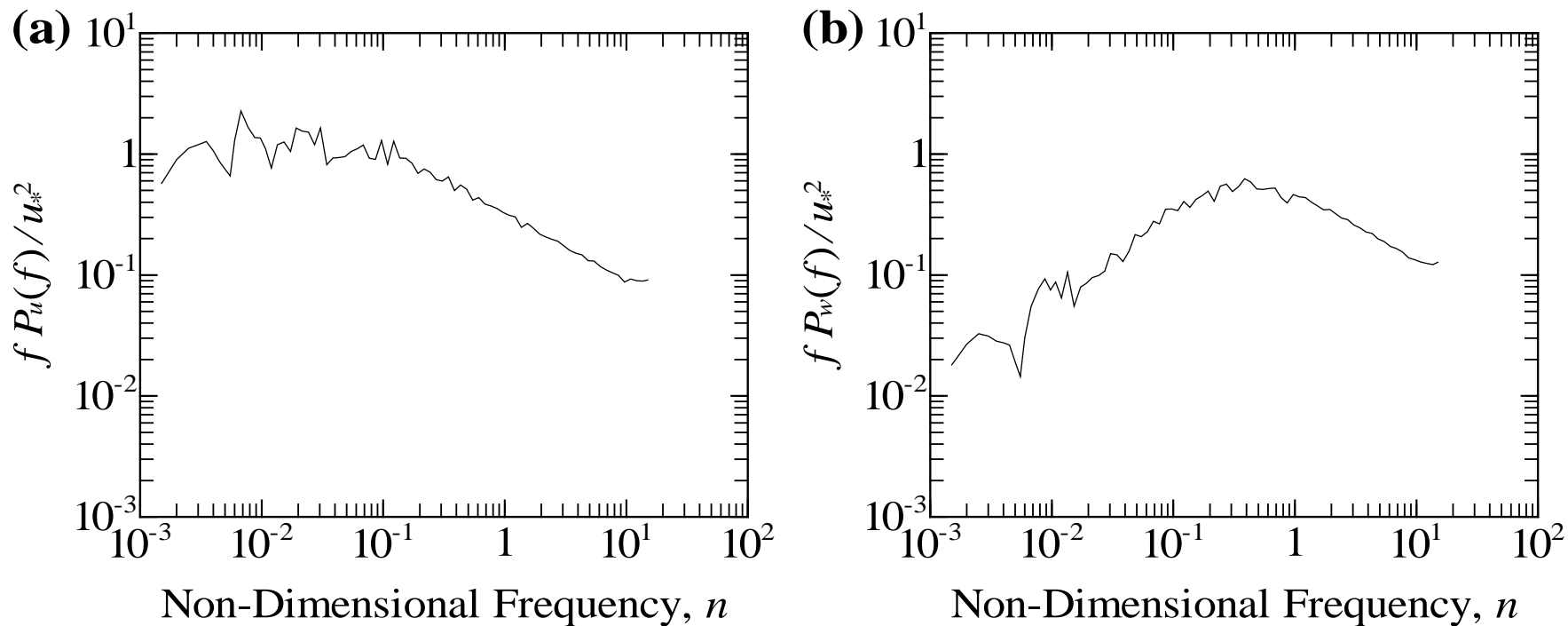
Fig. 2 Normalized power spectra for **a** the *u* velocity component and **b** the *w* velocity component averaged over parts 1–4 of the observational case on December 8, 1998 at Shionomisaki
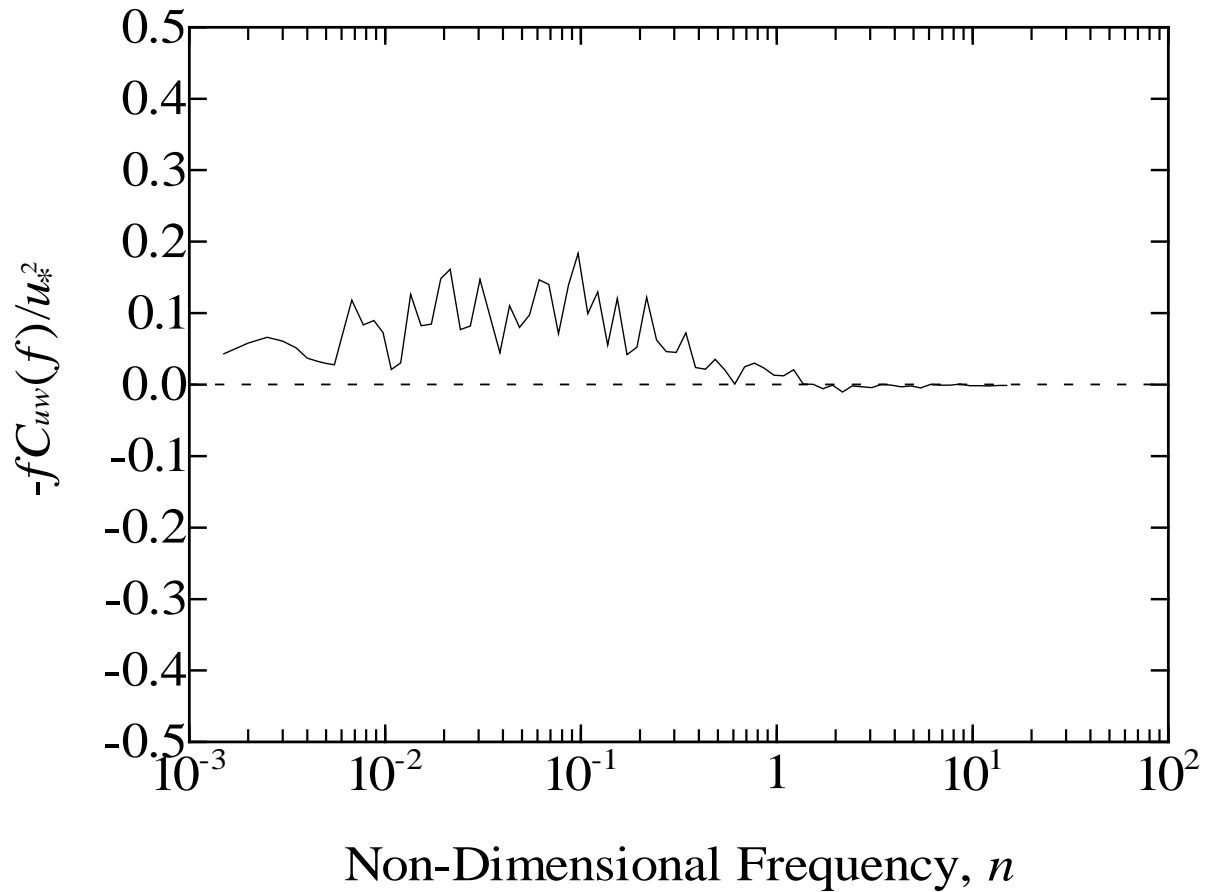
Fig. 3 Normalized cospectrum for the *u* and *w* velocity components averaged over parts 1–4 of the observational case on December 8, 1998 at Shionomisaki
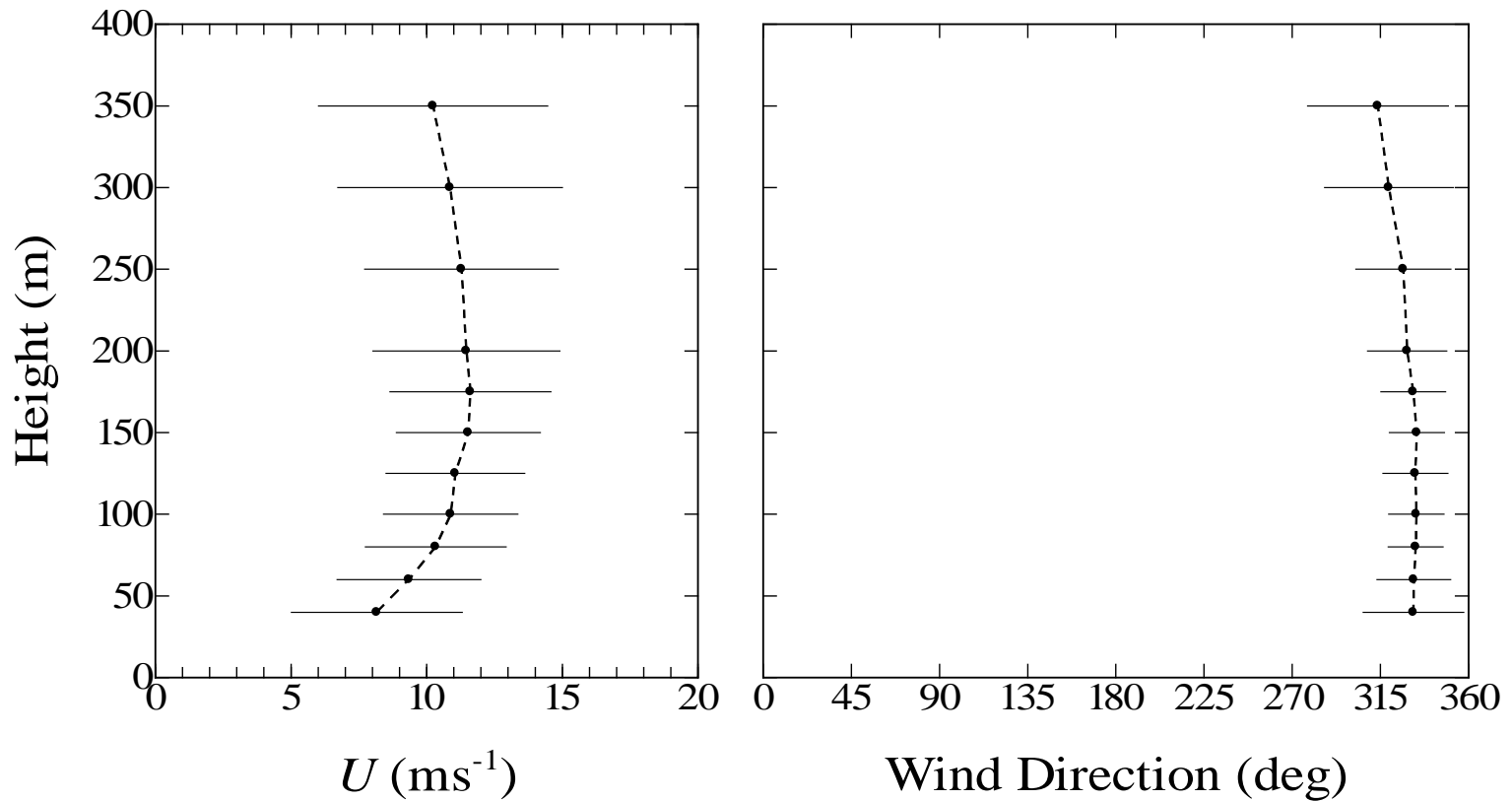
Fig. 4 Mean vertical profiles of horizontal wind speed (U) and wind direction measured by the Doppler sodar for part 1 of the observational case on December 8, 1998 at Shionomisaki. *Horizontal bars* denote the standard deviations from the mean values
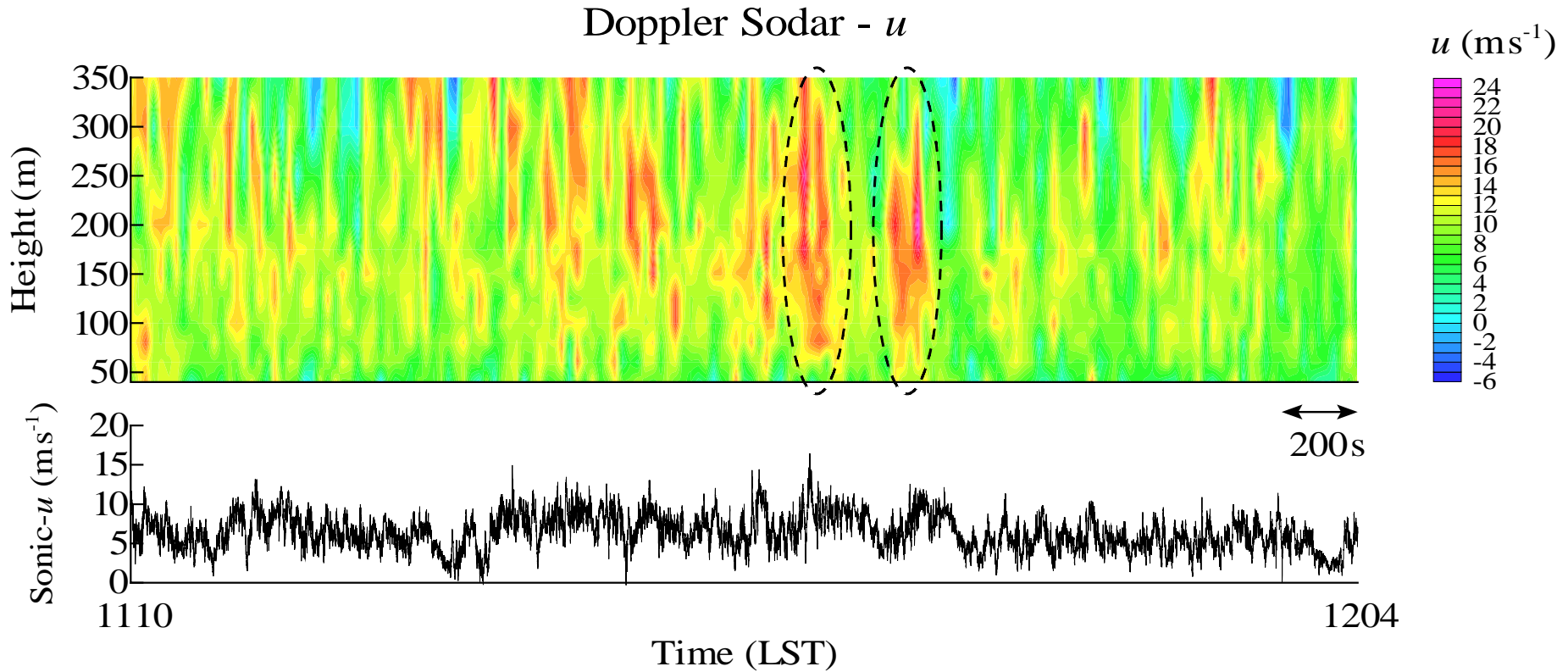
Fig. 5 (*Upper*) Time–height cross-section of the *u* velocity component observed by the Doppler sodar for part 1 of the observational case on December 8, 1998 at Shionomisaki. (*Lower*) Corresponding time series of the same velocity component measured by the sonic anemometer. The *arrow* denotes the time scale of 200 s, and the *dashed ellipses* denote typical large-scale regions of high velocity
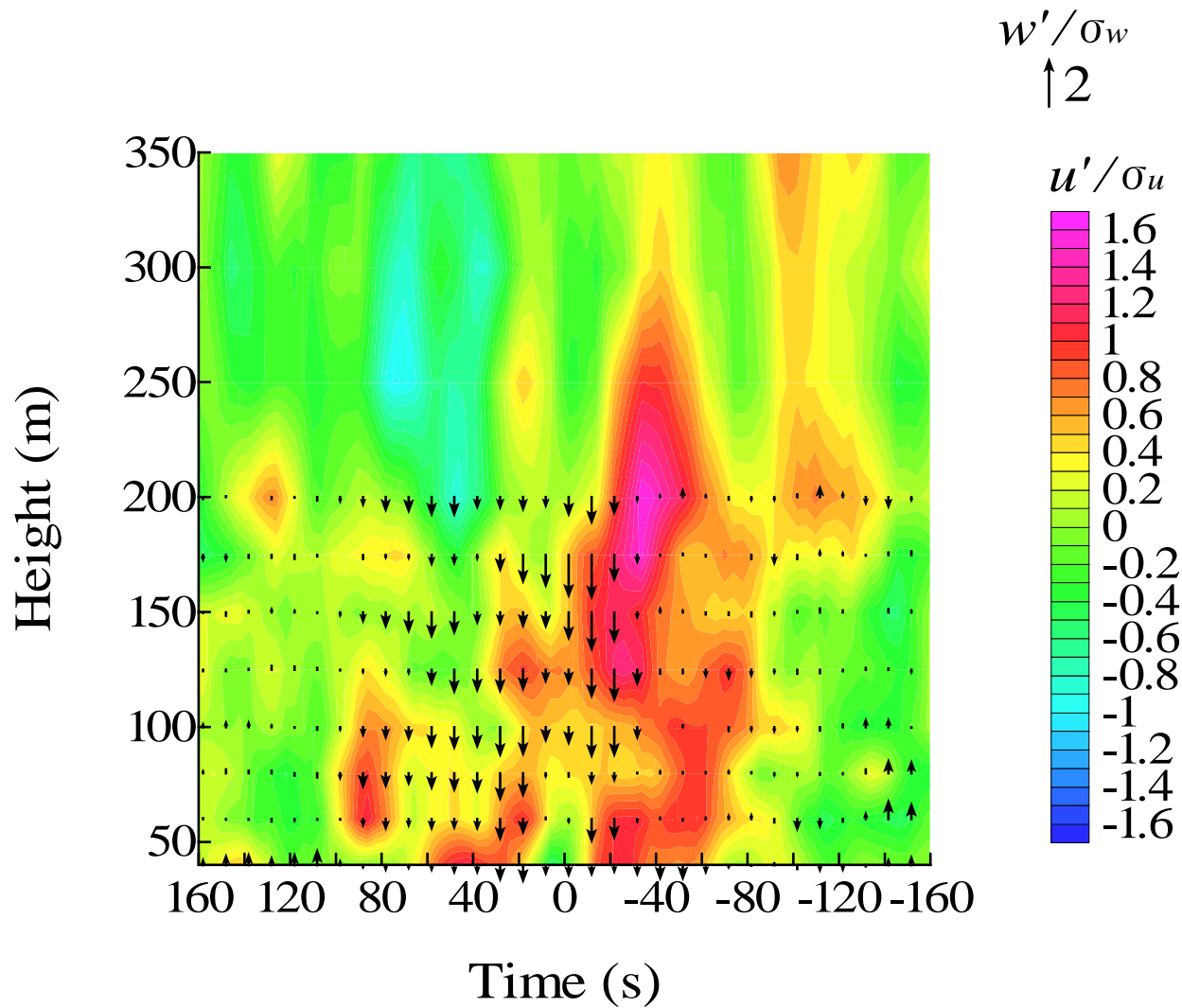
Fig. 6 Conditionally averaged wind pattern on a time–height cross-section (zero is the time of the detected events) for the observational case on December 8, 1998 at Shionomisaki. *Contours* indicate normalized *u'* values and *arrows* denote normalized *w'* values
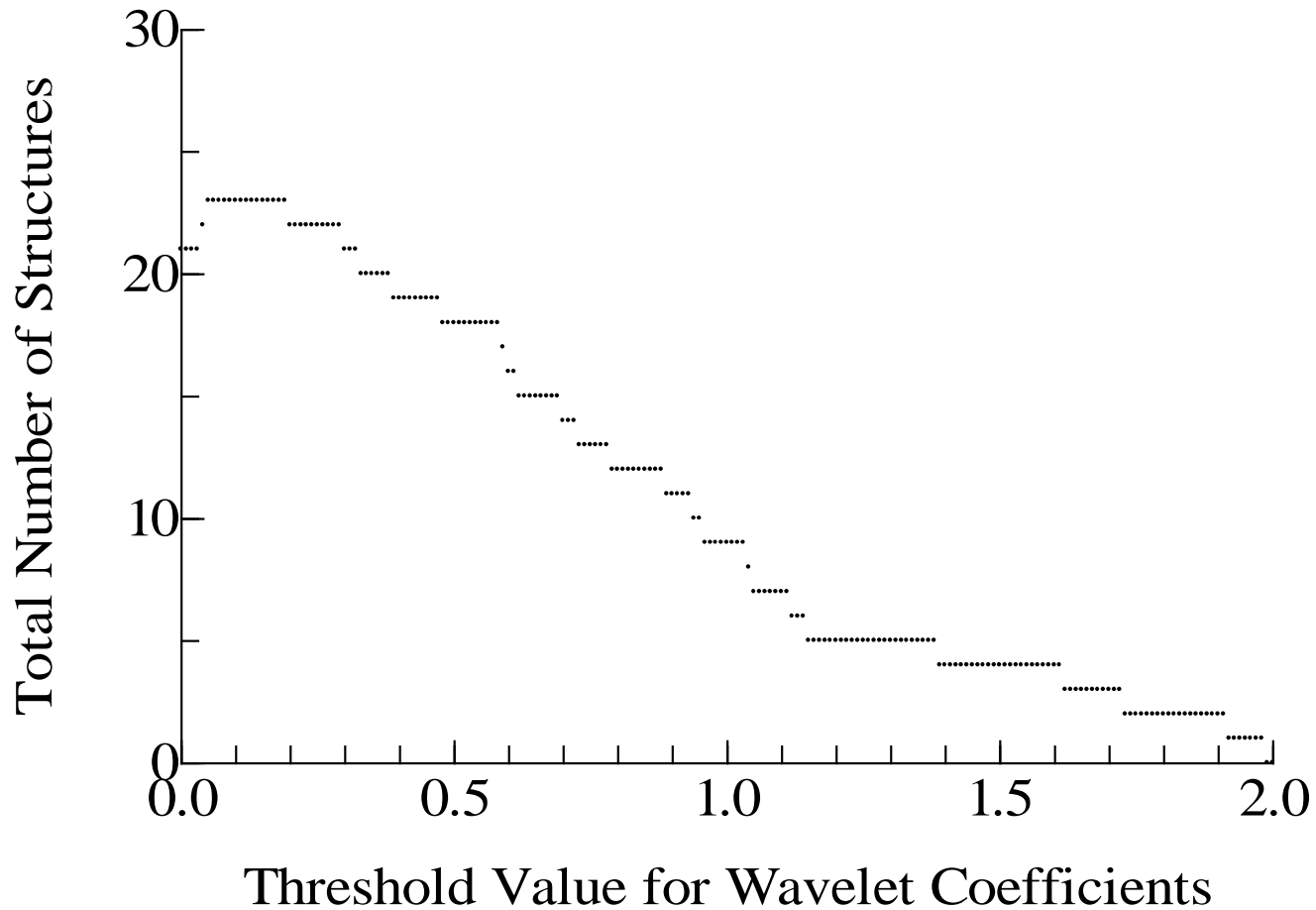
Fig. 7 Variation of the total number of high-speed structures with the threshold value (in increments of 0.01) for wavelet coefficients. This is examined for the sonic anemometer data in the case on December 8, 1998 at Shionomisaki
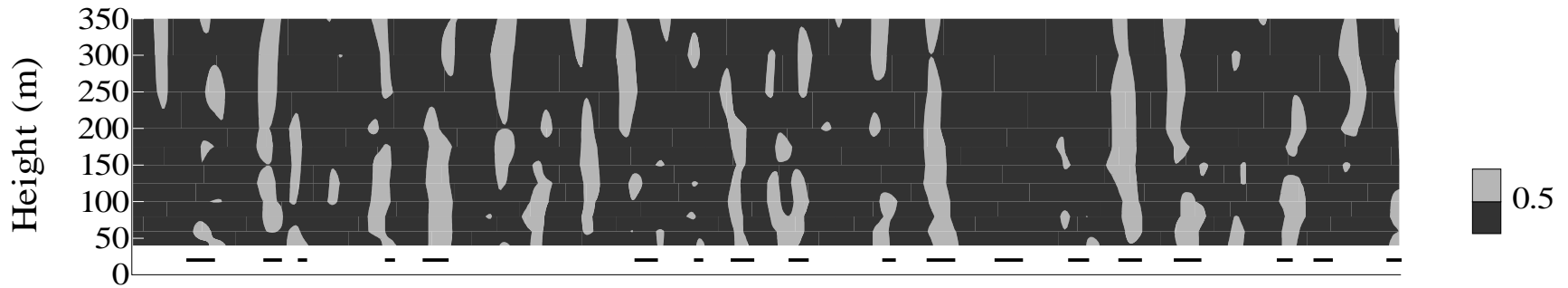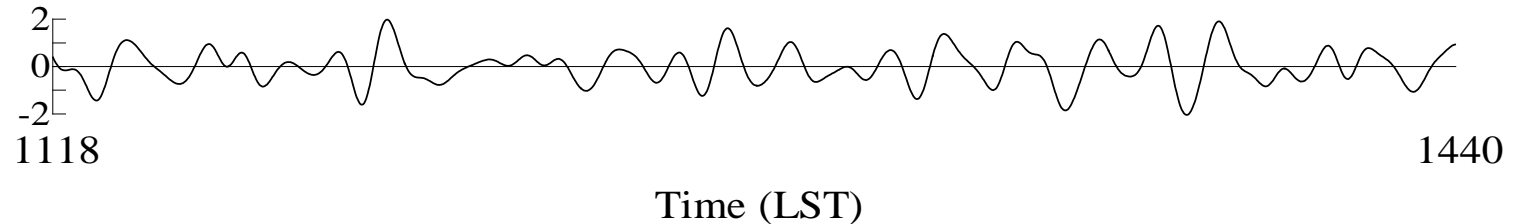
Fig. 8 (*Upper*) Time–height cross-section of wavelet coefficients for the *u* velocity component observed by the Doppler sodar on December 8, 1998 at Shionomisaki. (*Lower*) Corresponding time series of wavelet coefficients for the same velocity component measured by the sonic anemometer. *Areas of light tone* denote the regions in which the wavelet coefficient for the Doppler sodar data is larger than the threshold value, and *bold bars* show the periods during which the wavelet coefficient for the sonic anemometer data is larger than the threshold value
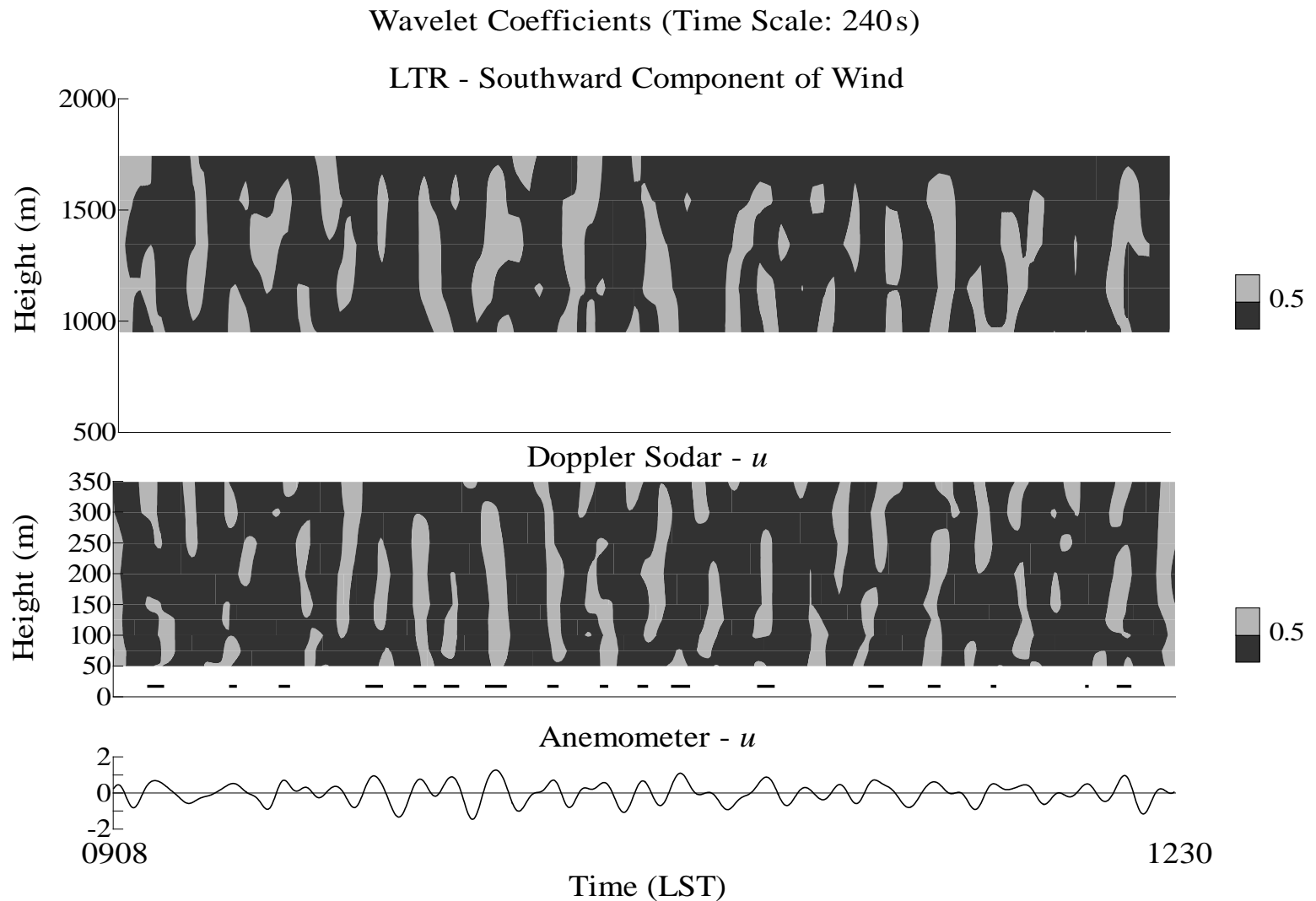
Fig. 9 (*Upper*) Time–height cross-section of wavelet coefficients for the southward component of wind observed by the lower troposphere radar (LTR) on December 10, 2001 at Shigaraki. (*Middle*) Corresponding section of wavelet coefficients for the *u* velocity component observed by the Doppler sodar. (*Lower*) Corresponding time series of wavelet coefficients for the *u* velocity component measured by the cup anemometer with the wind vane. *Areas of light tone* in the upper and middle figures denote the regions in which the wavelet coefficient is larger than the threshold value, and *bold bars* in the middle figure show the periods during which the wavelet coefficient for the anemometer data is larger than the threshold value
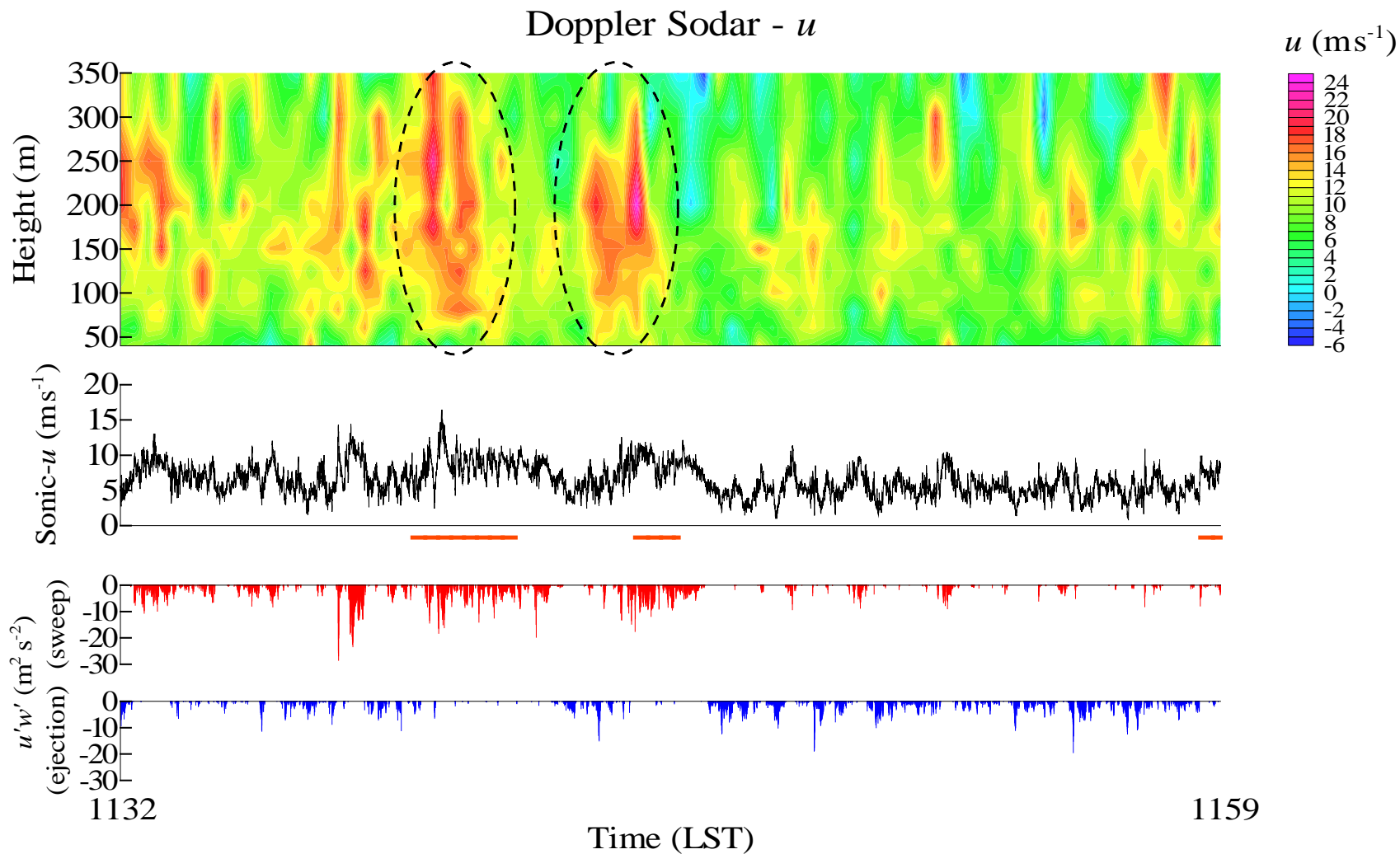
Fig. 10 (*Upper*) Time–height cross-section of the *u* velocity component observed by the Doppler sodar from 1132 to 1159 LST in part 1 of the observational case on December 8, 1998 at Shionomisaki. The *dashed ellipses* denote typical large-scale regions of high velocity. (*Middle*) Corresponding time series of the same velocity component measured by the sonic anemometer. The *bold bars* below the time series of *u* by the sonic anemometer show the periods during which the wavelet coefficient is larger than the threshold value. (*Lower*) Instantaneous $u'w'$ values at the times of ejection and sweep motions based on the sonic anemometer data